Efficient hydrogen evolution reaction with platinum stannide $PtSn_4$ *via* surface oxidation

Danil W. Boukhvalov, Andrea Marchionni, Jonathan Filippi, Chia-Nung Kuo, Jun Fujii, Raju Edla, Silvia Nappini, Gianluca D'Olimpio, Luca Ottaviano, Chin Shan Lue, Piero Torelli, Francesco Vizza and Antonio Politano, ***J. Mater. Chem. A****, 2020,**8**, 2349-2355* **DOI:** 10.1039/C9TA10097K

Efficient hydrogen evolution reaction with platinum stannide $PtSn_4$ via surface oxidation

Danil W. Boukhvalov[1,2], Andrea Marchionni[3], Raju Edla[4], Silvia Nappini[4], Jun Fujii[4], Chia-Nung Kuo[5], Gianluca D'Olimpio[6], Luca Ottaviano[6], Chin Shan Lue[5], Piero Torelli[4], Jonathan Filippi[3] and Antonio Politano[6,*]

1 College of Science, Institute of Materials Physics and Chemistry, Nanjing Forestry University, Nanjing 210037, P. R. China

2 Theoretical Physics and Applied Mathematics Department, Ural Federal University, Mira Street 19, 620002 Ekaterinburg, Russia

3 Consiglio Nazionale delle Ricerche (CNR)- Istituto di Chimica dei Composti OrganoMetallici (ICCOM), Area della Ricerca di Firenze, via Madonna del Piano 10, 50019 Sesto Fiorentino (Italy)

4 Consiglio Nazionale delle Ricerche (CNR)- Istituto Officina dei Materiali (IOM), Laboratorio TASC in Area Science Park S.S. 14 km 163.5 34149 Trieste, Italy

5 Department of Physics, National Cheng Kung University, 1 Ta-Hsueh Road, 70101 Tainan, Taiwan

6 Department of Physical and Chemical Sciences, University of L'Aquila, via Vetoio, 67100 L'Aquila (AQ), Italy

Abstract

By means of surface-science experiments, electrochemical tests and density functional theory, we unveil the mechanisms ruling the catalytic activity of $PtSn_4$. Specifically, through an investigation of the surface chemical reactivity toward CO, H_2O, O_2 molecules at room temperature and, moreover, of surface stability in air, we show that the catalytic activity of $PtSn_4$ is determined by the atomic tin layer constituting its surface termination. The $PtSn_4$ surface is not affected by CO poisoning, although it evolves into a tin-oxide skin in ambient atmosphere. We demonstrate that hydrogen evolution reaction for $PtSn_4$ can be modelled by the combination of two steps, i.e. Volmer and Tafel reactions. Surprisingly, surface oxidation induces a reduction of the energy barrier for the Tafel reaction, so that oxidized $PtSn_4$ behaves similarly to Pt(111), in spite of the reduced amount of Pt in the alloy and without available over-surface Pt sites. Correspondingly, we observe in electrochemical experiments a Tafel slope of 86 mV dec^{-1} and an onset potential similar to pure Pt. Our results indicate $PtSn_4$ as a promising novel material for electrocatalytic reactions, whose performance could be further tuned by surface treatments.

Corresponding author:

*antonio.politano@univaq.it

1 Introduction

Despite the excellent performances of platinum (Pt) in many catalytic reactions [1-3], the high cost (>30 US $/g) [4] and the restricted obtainability [5] of Pt make unavoidable the quest of economic and Earth-abundant potential alternatives [6-19]. One possible solution is to reduce Pt content by using Pt-based alloys [20-29], which also enable the exploitation of strain and ligand effects to enhance their chemical reactivity [30]. In particular, Pt-Sn alloys enable alkanes-alkenes conversion [31], although Pt-Sn alloys are mainly used for soldiery [32], electronic interconnections [33], jewelry [34], and dentistry [34]. Among Pt-Sn binary alloys, five stoichiometric compounds Pt_3Sn, PtSn, Pt_2Sn_3, $PtSn_2$, and $PtSn_4$ exist [35]. Recently, $PtSn_4$ single crystals have attracted particular attention for the presence of Dirac node arcs, i.e. closed loops formed by Dirac nodes in the momentum domain [36]. From the analysis of transport experiments in Ref. [37] one can estimate an electrical conductivity at room temperature of $2.5 \cdot 10^5$ S/m, which is increased by a 10^3 factor at T=2 K. Therefore, $PtSn_4$ can be suitably used as electrode in electrochemistry, also in consideration of the carrier density $n \simeq 2.6 \times 10^{28}$ m^{-3} (comparable with its value in copper $\simeq 8.9 \times 10^{28}$ m^{-3} [38]). Very recently, the suitability of $PtSn_4$ for hydrogen evolution reaction (HER) has been evidenced [39], although the mechanism ruling HER activity remains largely unclear.

While the preparation of $PtSn_4$ nanoparticles is challenging, due to the formation of Pt-Sn binary phase [40], large-size $PtSn_4$ single crystals can be efficiently grown by flux method [37], enabling the potential industrial scale-up of $PtSn_4$-based applications. However, the use of $PtSn_4$ in electrocatalysis and nanoelectronics requires control on surface properties, including chemical activity, surface termination, surface reconstruction etc. It should be noted that also the emergence itself of Dirac node arcs is associated to the surface states [36] and, accordingly, it is strictly connected to the composition of surface termination, to date not determined for $PtSn_4$. Unfortunately, surface-science investigations on $PtSn_4$ are missing yet. The lack of information about surface properties represents a severe hurdle to understand and tailor surface catalysis based on $PtSn_4$.

Here, we combine high-resolution X-ray photoelectron spectroscopy (XPS), scanning tunneling microscopy/spectroscopy (STM/STS) and high-resolution electron energy loss spectroscopy (HREELS) with density functional theory (DFT) to clarify the key features of chemical reactivity of $PtSn_4$ surfaces toward ambient gases. Specifically, we discover that the termination of the as-cleaved surface is an atomic layer of Sn exhibiting a high CO tolerance. However, the surface is unstable in oxygen environment and in air, with the emergence of a tin-oxide skin, which plays a surprisingly crucial role in the reduction of the energy barrier of the Tafel step of HER to values near to the case of pure Pt, thus opening novel scenarios for catalysis in oxidative environments.

2 Results and Discussion

Single crystals of $PtSn_4$ have been grown according to experimental procedures reported in the Methods section (see also Supporting Information, SI, Fig. S1, for X-ray diffraction experiments). The determination of the surface termination is crucial to achieve control over surface phenomena, since the outermost layer of the crystal mostly determines surface chemical reactivity [41, 42]. Specifically, three possible surface terminations can be realized for the natural cleavage plane, i.e. the (010) surface. The first possibility is to have a Sn-terminated surface, in which the Pt subsurface layer is located between two Sn layers (2Sn-termination), as in the bulk crystal of $PtSn_4$, whereas the second scenario is a Pt-terminated surface with nearest Pt atoms distant 0.45 nm, as sketched in Fig. 1a. A third possibility is a 1Sn-termination, with a single Sn atomic surface layer on top of an underlying layer of Pt atoms (Fig. 1b). Note that two Sn-terminated surfaces in Fig.1a-b have identical crystal structure of the top layer (with nearest Sn atoms distant 0.34 nm), although the presence of the Pt-sublayer should be accounted in the assessment of the catalytic properties of Sn-terminated surfaces.

Calculations of the total energies of both slabs displayed on Figs. 1a,b indicate that the formation of 1Sn-terminated surface is more energetically favorable by about 0.155 eV per single Sn-atom on the

surface ($1.5 \cdot 10^{16}$ kJ/cm^2) than the formation of (010)-oriented Pt termination and 2Sn-terminated (0-10) sides.

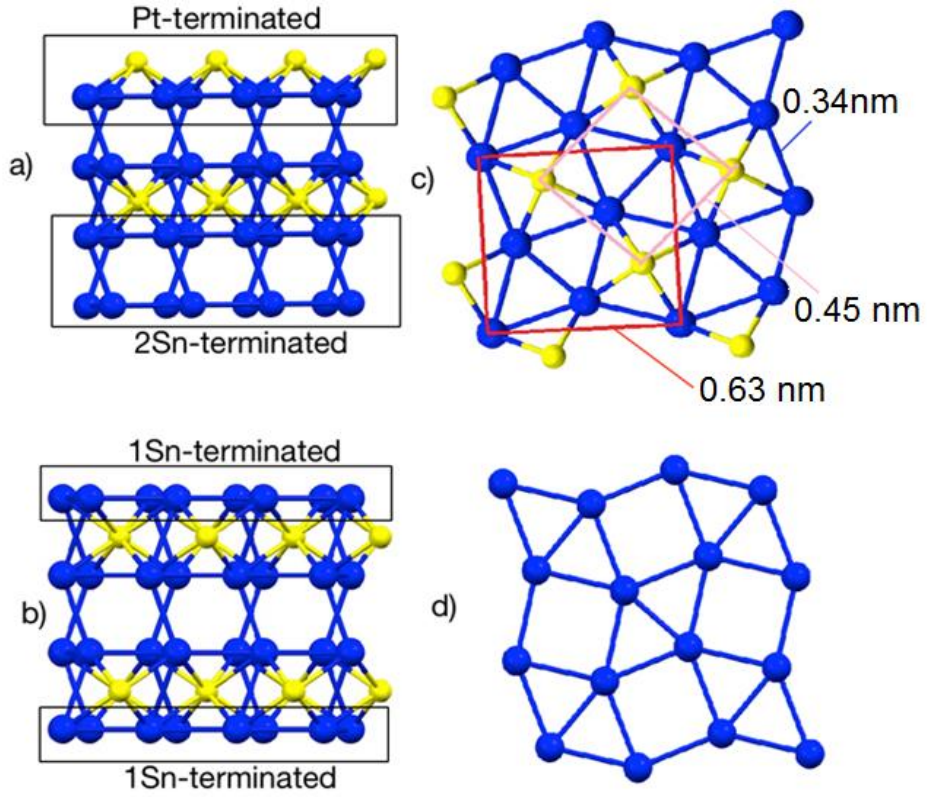

Figure 1. Side view of the different possible surface terminations of $PtSn_4$(010): (a) with an outermost platinum atomic layer (Pt-terminated) and with bilayer Sn (2Sn-terminated) ; (b) with an outermost single atomic layer of tin (1Sn-terminated). Panels (c) and (d) illustrate the top view of the Pt-terminated surface and the top layer of both types (1Sn and 2Sn) of tin-terminated surfaces, respectively.

Figure 2a displays the low-energy electron diffraction (LEED) pattern of as-cleaved $PtSn_4$. The atomic resolution image obtained by scanning tunneling microscopy (STM, Fig. 2b) and its corresponding fast-Fourier transform (FFT, Fig. 2c) are consistent with the square lattice identified by LEED. According to both STM and quantitative LEED analyses, the surface unit cell is 0.33 x 0.33 nm, in agreement with the lateral dimension of a Sn-terminated surface.

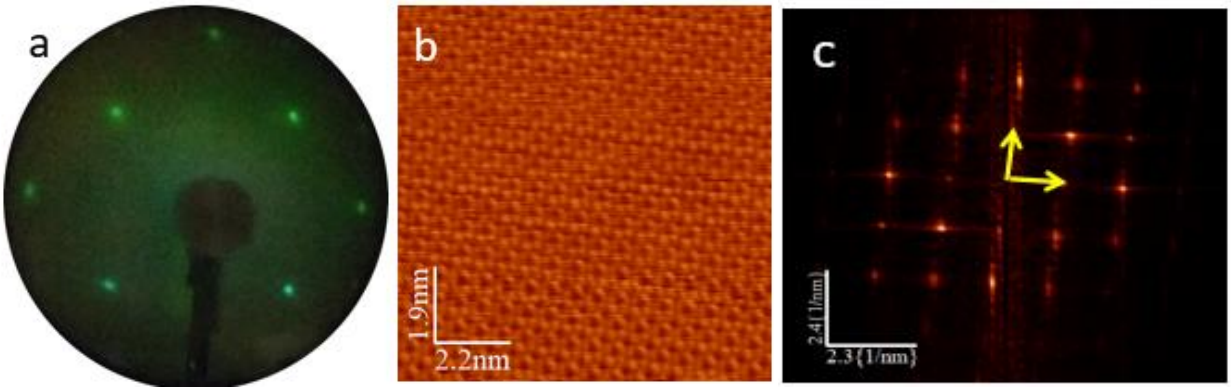

Figure 2. (a) LEED pattern of $PtSn_4$(010), acquired with an impinging energy of 44 eV. (b) Constant current STM image. (V= +620 mV, I=0.7 nA) (c) 2D FFT of the STM image. The yellow arrows denote the unit vectors.

The compositional depth profile of the $PtSn_4$ surface probed by energy-dependent and angle-dependent X-ray photoelectron spectroscopy (XPS, see SI, Section S3) indicates the occurrence of 1Sn-terminated surface.

For the sake of completeness, it is worth mentioning that the authors of Ref. [39] assume that the $PtSn_4$ surface has a Pt termination due to the similar HER activity with respect to pure Pt, in contrast with the conclusions of our detailed surface-science investigation concerning surface termination, with subsequent differences also for the catalytic mechanisms.

The analysis of core-level spectra measured with XPS is crucial in order to assess surface chemical reactivity of $PtSn_4$. Pt-4f and Sn-3d core levels measured for the as-cleaved surface and after exposure to 45 kL (1 L=10^{-6} Torr·s) of CO, H_2O and O_2 are shown in Figs. 3a-b, respectively. The values of the binding energies (BE) of Pt-4f core levels of the as-cleaved $PtSn_4$(010) surface (~75.3 for $4f_{5/2}$ and ~72.0 eV for $4f_{7/2}$) are shifted by +1.0 eV compared to Pt(111) [43] and +0.5 eV compared to Pt-skin-terminated Pt_3Ni(111) [44]. The blue-shift of the Pt-4f components to higher BEs with respect to pure Pt surfaces can be ascribed to the presence of Pt-Sn bonds, as previously observed on other Pt-based alloys [45]. Concerning Sn-3d, the as-cleaved sample has a doublet with BEs centered at 485.2 eV ($3d_{5/2}$) and 493.7eV ($3d_{3/2}$), which can be associated to Sn atoms in the bulk [46, 47] (Fig. 3b).

XPS experiments on CO-dosed $PtSn_4$ clearly show that, in spite of the presence of Pt atoms in the crystal structure, the surface is fully tolerant toward CO adsorption. As a matter of fact, no changes in the line-shape of Pt-4f core levels was detected, proving no trace of CO adsorption on Pt sites. A careful inspection of Sn-3d core levels reveals a small contribution (8% of the total spectral area) at ~486.2 eV for Sn-$3d_{5/2}$, which can be assigned to SnO species resulting from the early stage of tin-oxide formation (SnO/SnO_{ads}), arising from the decomposition of CO molecules at Sn sites in the nearness of edges [47] . Correspondingly, the O-1s core level (SI, Fig. S3) shows SnO contribution at ~530.3 eV[47]. To provide further evidence of CO tolerance of $PtSn_4$, we carried out a vibrational investigation by high-resolution electron energy loss spectroscopy (HREELS). Vibrational experiments (SI, Fig. S4) confirm (i) the occurrence of dissociative CO adsorption at defect sites with SnO formation and (ii) the absence of molecular adsorption of CO. These findings prove that $PtSn_4$ could represent a perfectly CO tolerant electrode, contrary to other Pt-based alloys (see the comparison with the case of Pt_3Ni in SI, Section S7).

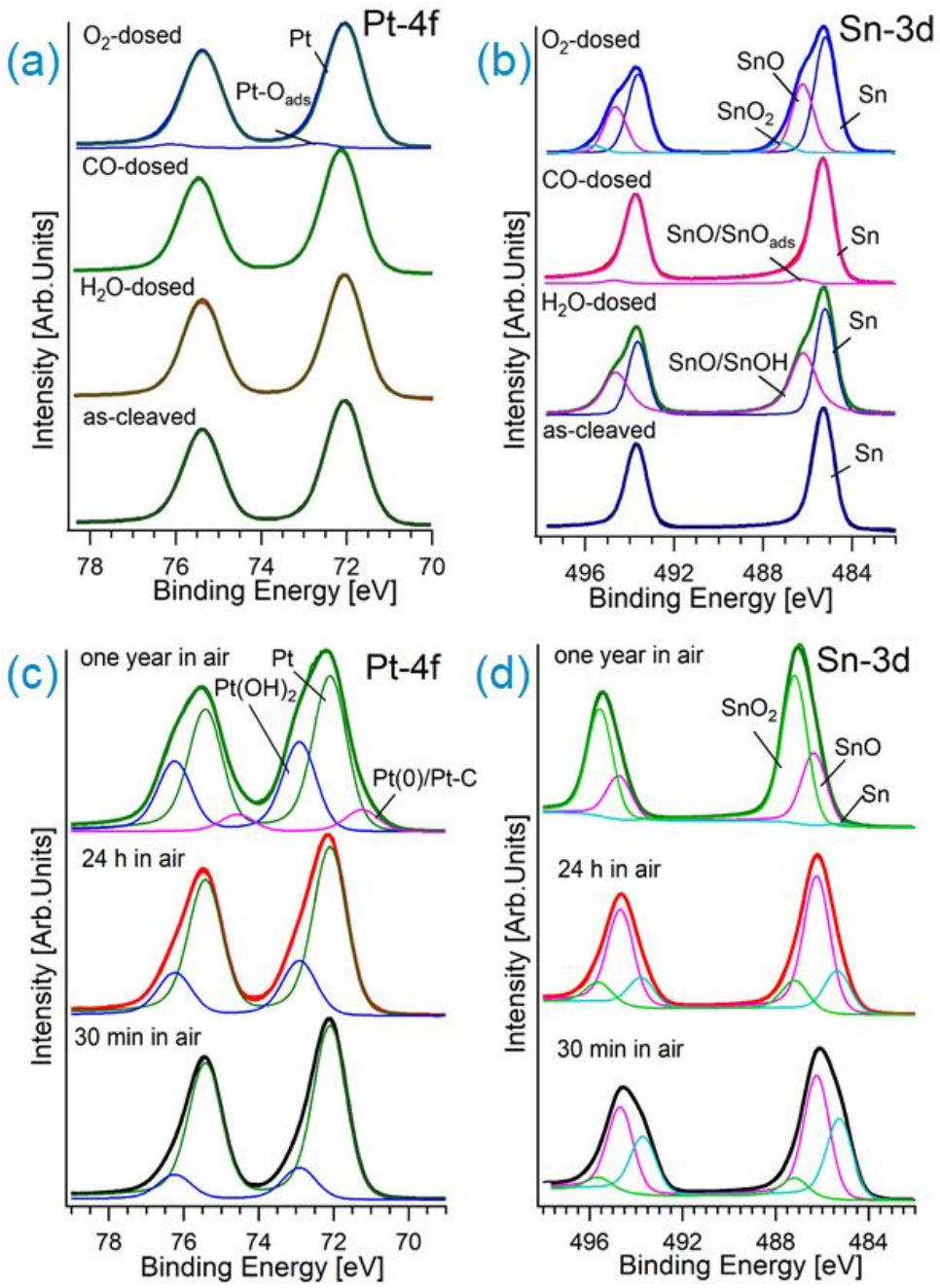

Figure 3. Core-level spectra for (a, c) Pt-4f and (b, d) Sn-3d for (a, b) as-cleaved, CO-dosed, H_2O-dosed, and O_2-dosed $PtSn_4$ and (c, d) $PtSn_4$ exposed to air for 30 minutes, 24 hours, and one year. The photon energy is 800 eV and the spectra are normalized to the maximum.

When $PtSn_4$ is exposed to H_2O and O_2, both oxidation and water or O-fragments adsorption selectively involve only Sn atoms. Specifically, no additional features in Pt-4f core levels are present, except a negligible contribution from $Pt\text{-}O_{ads}$ (4 %) in the O_2-dosed sample [48] (Fig. 3a). Sn-3d core-level spectra (Fig. 3b) show the presence of a component ascribable to SnO/Sn-OH species (BE of

~486.2 eV) in the H_2O-dosed surface[47] , while a further component due to SnO_2 (BE of ~487.2 eV) [47] is observed in the O_2-dosed sample. In the H_2O-dosed sample, oxide and hydroxide components (SnO/Sn-OH) are ~25% of Sn-3d total area. In the case of O_2-dosed $PtSn_4$, the oxidation is dominated by both SnO (35%) and SnO_2 (6%) components. The analysis of O-1s core level is fully consistent with the picture emerging from Pt-4f and Sn-3d data (See SI, Fig. S3).

By means of a quantitative XPS analysis[49], the thickness of the tin-oxide layer in H_2O-dosed and O_2-exposed samples is estimated to be 6.6±0.9 and 7.2±1.0 Å, respectively. Therefore, we can infer that a sub-nanometric tin-oxide skin protects the underlying $PtSn_4$ bulk crystal from the interaction with the environment, with only negligible effects on the first atomic layer of Pt.

With the aim to assess aging phenomena, we have monitored the evolution of core levels as a function of the time of the exposure at ambient atmosphere (Figs. 3c-d). We observe that, in a timescale extended up to one year in air, the SnO_2 component (Fig. 3d) gradually increases from 5% (after 30 min in air) to 13% (after 24 h in air) and finally to 65% (after 1 year in air) with the corresponding disappearance of Sn(0) species. The thickness of the tin-oxide layer (SnO+SnO_2) formed on the sample stored in ambient atmosphere has the following temporal evolution: 9±1 Å (30 min in air), 14±2 Å (24 h in air), and 36±5 Å (1 year in air). Consistently, the component associated to $Pt(OH)_2$ after one year reaches up to the 35 % of the area of the Pt-4f core level (Fig. 3c) and, moreover, a small contribution of Pt(0) appears at 71.2 eV[50] (Fig. 3c). The presence of this component can be explained by considering that the reaction $PtSn_4 + 4O_2 \rightarrow Pt + 4SnO_2$ is energetically favorable, as indicated by the values of the differential enthalpy ΔH, which are -4.78 and -3.41 eV for Pt-rich and Sn-rich surfaces, respectively.

The eventual effects of chemisorption and oxidation on electronic properties were assessed by measuring the valence band (SI, Fig. S5), finding that surface treatments and air exposure only produced minimal effects.

Experimental results were validated by a theoretical model of surface chemical reactivity. We considered the energetics of physical adsorption and further decomposition of all the gases (CO, O_2 and H_2O) on Pt-, 1Sn- and 2Sn-terminated surfaces. For the most energetically favorable 1S-terminated surface, we also check the influence of Sn-vacancy sites in surface layer (SI, Fig. S7b) and of Pt vacancies in the subsurface layer. Calculations (see Tab. I) indicate a negative value of the differential free energy of physisorption of CO only for the Pt-terminated surface. The absence of any traces of CO in experimental spectra (XPS in Fig. 3a and HREELS in Fig. S4 of the SI) suggests the occurrence of a Sn-terminated surface. Physical adsorption with further decomposition of molecular oxygen is favorable for each possible termination. In the case of Sn-terminated surface, the magnitude of differential free energy of physical adsorption of O_2 is rather small (-2.5 and -0.5 kJ/mol for 1Sn- and 2Sn-terminated surfaces, respectively), which corresponds to metastable adsorption. The presence of defects (especially, Sn vacancies in surface layer) provides stabilization of molecular oxygen on the surface. Decomposition of water is unstable on all types of surfaces. Therefore, water environment is safe for $PtSn_4$.

As the energy cost of the physical adsorption of chemical species on the 1Sn-terminated $PtSn_4$ surface is rather low, we assess its suitability for electrochemical reactions by a model, which also considers the effects of the hydrogen coverage. Firstly, we study the combination of Volmer ($H^+ + e^- \rightarrow H_{ads}$) and further Heyrovsky ($H_{ads} + H^+ + e^- \rightarrow H_2$) reactions. Calculations (SI, Fig. S8a) evidence that the second step is energetically costly (more than 0.5 eV) and neither oxidation nor hydrogenation of the surface significantly influence the energetics of HER. Therefore, we also consider an alternative pathway of HER, involving the combination of the Volmer step with the Tafel reaction ($2H_{ads} \rightarrow H_2$) between two adsorbed hydrogen atoms. In the case of unoxidized 1Sn-terminated surface, the energy barrier for the Tafel reaction is 0.25 and 0.60 eV for a pair of hydrogen atoms and for the totally hydrogenated surface, respectively. In the case of the oxidized surface, adsorption of hydrogen atoms is possible on both Sn- and O-sites (see SI, Fig. S7c for a visualization). The energy barriers for two, four, six and eight hydrogen atoms per supercell is 0.98, 0.12, 0.25 and 0.18

eV, respectively. Notably, the energy barrier assumes values closer to the case of Pt(111) (about 0.1 eV), although defects increase the energy cost of Heyrovsky reaction [18] with subsequent reduction of the overall efficiency on realistic surfaces.

Table I. Calculated differential enthalpy and Gibbs free energies (in kJ/mol) for physical adsorption and decomposition of the molecules of CO, O_2 and H_2O on Pt- and Sn-terminated surfaces of $PtSn_4$.

Surface termination	Adsorbant	Physical adsorption		Decomposition
		ΔH [kJ/mol]	ΔG [kJ/mol]	ΔH [kJ/mol]
1Sn	CO	+6.6	+26.0	—
	O_2	-13.8	-2.5	-155.5
	H_2O	+6.4	+36.7	+44.4
1Sn with one Sn vacancy	CO	-12.2	+7.2	—
	O_2	-25.6	-14.3	-297.2
	H_2O	-10.7	+19.6	+74.9
1Sn with one Pt vacancy	CO	-0.2	+19.2	—
	O_2	-14.8	-3.5	-148.2
	H_2O	+5.9	+37.2	+37.8
Pt	CO	-134.5	-115.1	+482.1
	O_2	-79.4	-68.1	-228.7
	H_2O	-58.5	-27.2	+85.3
2Sn	CO	-5.3	+14.0	—
	O_2	-11.8	-0.5	-27.47
	H_2O	+6.5	+36.8	+124.2

On the other hand, oxygen evolution reaction (OER) on both Pt- and 1Sn-terminated surfaces has an energy profile similar to pure Pt (Fig. S8b). Upon oxidation of the 1Sn-terminated surface, no available site is available for further adsorption of hydroxyl groups, thus making oxidized $PtSn_4$ unsuitable for OER.

To validate $PtSn_4$ as a candidate for HER and OER, we performed electrochemical tests (see Methods). Cyclic voltammetries (CVs) show performances resembling more to the Pt rather than to the

Sn polycrystalline foil (Fig. 4a). Notably, $PtSn_4$ exhibits values of onset potentials for HER and OER very close to Pt values, with also similar shape of the cycles.

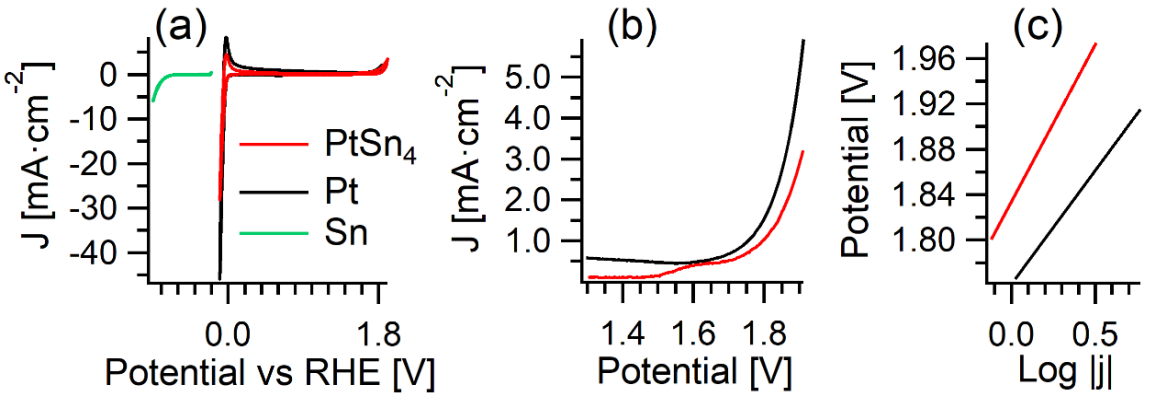

Figure 4. (a) CV of $PtSn_4$ (red curve), Pt foil (black curve) and Sn foil (green curve). The scan speed is 50 mV s^{-1}. The upper potential of Sn foil is limited by tin dissolution, in agreement with the Pourbaix diagram [51]. (b) Linear sweep voltammetry on $PtSn_4$ (red curve) and Pt (black curve) samples between 1.3 and 1.9 V vs RHE (reversible hydrogen electrode) at 20 mV s^{-1}. (c) Tafel plot of $PtSn_4$ (red line) and Pt (black line), acquired at 1 mV s^{-1}.

Interestingly, such a similarity in HER only appears whenever the $PtSn_4$ surface is exposed to a potential higher than 1.035 V vs RHE (SI, Section S10). We measured the Tafel slope for pristine sample and after a treatment at 1.035 V. As reported in Fig. S5, the slopes are 442 and 86 mV dec^{-1}, respectively, thus confirming the improvement of HER kinetics after surface oxidation, consistently with our theoretical model. Indeed, its value for the pristine surface (after polishing treatment) is in good agreement with a Sn-terminted surface due by the high energy barrier (0.6 eV). After the oxidizing electrochemical treatment, during cycling voltammetry, the Tafel slope decreased to 86 mV dec^{-1} probably due to the oxidized tin species on the surface, as predicted by the computational model. However, the oxidation process may introduce defects on the surface that could increase the energy barrier for the Heyrovsky reaction. It results in a higher Tafel slope compared to theoretical Pt value.

To test the long-term stability of the electrode towards HER, we performed a chronoamperometric experiment at -44 mV vs RHE (SI, Fig. S11). The absolute value of the current density decreased from ~1 to 0.14 mA cm^{-2} in a few minutes. Successively, the performance slightly decreased until to reach ca. -0.08 mA cm^{-2} and remained stable.

Concerning the OER behavior, the linear sweep voltammetry showed that $PtSn_4$ has a similar onset potential than Pt, between 1.6 and 1.7 V, although with lower current density (Fig. 4b). The weak current peak around 1.5 V for $PtSn_4$ should be associated to the formation surface tin-oxide phases. Remarkably, Tafel slopes (Fig. 4c) of both Pt and $PtSn_4$ electrodes are very similar (200 and 232 $mV \cdot dec^{-1}$, respectively). The long-term stability test towards OER was tested with a chronoamperometric experiment at 1.8 V vs RHE (SI, S20). The current quickly decreased in a few minutes (from 1.9 to 0.9 mA cm^{-2}). Successively, the performance slightly grown up to reach a value approx. 1.8 mA cm^{-2} and after ca. 6-7 hours remained stable.

3 Conclusions

We have found that $PtSn_4$ is terminated with an atomic layer of Sn, which makes the surface fully tolerant to CO molecules. Oxidation of $PtSn_4$ surface occurs via the formation of a tin-oxide skin, whose thickness is limited to a few nanometers even after one year in air. However, surface oxidation is unexpectedly beneficial for catalysis. As a matter of fact, it decreases the energy barrier of the Tafel step of HER to values near to theoretical expectations for Heyrovsky step of HER on the Pt(111) surface. Therefore, $PtSn_4$ exhibits performances in HER and OER in acidic environment similar to pure Pt, in spite of a reduced content of the precious Pt element and without over-surface Pt sites.

Novel concepts related to the enhancement of catalytic activity via surface oxidation are expected to open new avenues for catalysis in oxidative environments, also considering that they can be applied to other materials with similar physicochemical and structural properties. Moreover, it is evident that the catalytic activity of oxidized $PtSn_4$ could be easily optimized by appropriate surface treatments,

although achieved performances in HER are already competitive with state-of-the-art materials (pure Pt).

Methods

Single-crystal growth and cleavage

Single crystals of $PtSn_4$ were synthesized by the self-flux method. High-purity Pt foil (99.99%) and Sn ingots (99.999%) were mixed in the ratio of 1:25 and sealed in an evacuated quartz tube with a flat bottom. The mixed elements were heated to 600 °C for 6 hours, dwelled for 10 hours, quickly cooled to 350 °C in 5 hours, and then slowly cooled at a rate of 1°C/h to 250 °C. Subsequently, the excess Sn flux was removed by centrifugation and then etched in concentrated hydrochloric acid. The $PtSn_4$ crystals were cleaved in ultra-high vacuum (UHV) by post-method with natural cleavage plane coinciding with the (010) orientation. Surface cleanliness was checked by XPS (SI, Fig. S2) and vibrational spectroscopy, while surface crystalline order was checked by LEED and STM.

XPS

XPS experiments were performed at the APE-HE beamline of the Elettra Synchrotron, Trieste, Italy. XPS spectra were acquired with an Omicron EA125 hemispherical electron energy analyzer, with the sample at room temperature and in normal emission condition. The linearly polarized light was impinging on the sample forming an angle of 45 degrees with respect to the normal to the surface. Gas inlet of carbon monoxide, water and oxygen was performed by using leak valves at a common exposure at a pressure of 10^{-4} mbar for 10 min, corresponding to 45 kL (1 L=$1 \cdot 10^{-6}$ Torr·s). Fit procedures of XPS spectra were carried out following procedures described in SI, Section S11.

STM

STM analysis was conducted using a home-built UHV STM apparatus connected to the APE beamline with UHV transfer system. The STM topography image was taken with constant current mode. The bias voltage was applied on the sample.

DFT calculations

The atomic structure and energetics of various configurations was studied by DFT using the QUANTUM-ESPRESSO code [52] and GGA–PBE [53], taking into account van der Waals forces correction[54]. For all calculations, we used ultrasoft pseudopotentials [55]. The values of energy cutoffs of 25 and 400 Ry for the plane-wave expansion of the wave functions and the charge density, respectively. Total energies of gases were calculated for the single molecule in an empty box. The total energy of Pt for Pt-rich conditions is defined by the formula: $E(Pt) = 4E(Sn) - E(PtSn_4)$, where E(Sn) is the total energy of bulk metallic tin. For computing the total energy of Sn, a similar procedure was used. The differential enthalpy of reaction is defined as difference in calculated total energies of products and reactant. Thus, negative differential enthalpy corresponds with exothermic reactions.

Physisorption enthalpies were calculated by the standard formula:

$\Delta H_{phys} = [E_{host+mol} - (E_{host} + E_{mol})]$,

where E_{host} is the total energy of pristine surface, and E_{mol} is the energy of the single molecules of selected species in an empty box. In the case of water adsorption, we only considered the gaseous phase. Decomposition energy is defined as difference between the total energy of the system with adsorbed molecule and the total energy of same system after decomposition of the same molecule on the surface. For the case of physisorption, we also evaluated differential Gibbs free energy by the formula:

$\Delta G = \Delta H - T\Delta S$,

where T is the temperature and ΔS is the change of entropy of adsorbed molecule, which was estimated considering the gas→liquid transition by the standard formula:

$\Delta S = \Delta H_{vaporisation}/T$,

where $\Delta H_{vaporization}$ is the measured enthalpy of vaporization.

Electrochemical tests

Electrochemical experiments were conducted in a common three electrodes glass cell equipped with

Pt wire as counter electrode and $Ag/AgCl/KCl_{sat}$ as reference electrode and all the potentials were referred to the RHE. Equipment was cleaned with a mix of water and 2-propanol and rinsed several times with ultrapure water (18.2 MΩ). A 0.05 M solution of sulfuric acid (99.9%, Sigma Aldrich) in ultrapure water was used as electrolyte. The electrochemical experiments were conducted with a Priceton Applied Research (PAR) PARSTAT 2277 potenziostat galvanostat. All current measurements were normalized to the geometric surface area of each electrode. CVs experiments were conducted at 50 mV s^{-1}, otherwise stated. Slow linear sweep experiments to obtain the Tafel slope were conducted at 1 mV s^{-1}.

Acknowledgments

AP thanks Sincrotrone Elettra S.C.p.A. for financial support. DWB acknowledges support from the Ministry of Education and Science of the Russian Federation, Project №3.7372.2017/БЧ.

Bibliography

1. Z. P. Xiang, H. Q. Deng, P. Peljo, Z. Y. Fu, S. l. Wang, D. Mandler, G. Q. Sun and Z. X. Liang, *Angew. Chem.*, 2018, **130**, 3522-3526.
2. J. Greeley, I. Stephens, A. Bondarenko, T. P. Johansson, H. A. Hansen, T. Jaramillo, J. Rossmeisl, I. Chorkendorff and J. K. Nørskov, *Nature Chem.*, 2009, **1**, 552.
3. K. Ding, A. Gulec, A. M. Johnson, N. M. Schweitzer, G. D. Stucky, L. D. Marks and P. C. Stair, *Science*, 2015, **350**, 189-192.
4. R. Sari, S. Hammoudeh and U. Soytas, *Energy Economics*, 2010, **32**, 351-362.
5. E. Alonso, F. R. Field and R. E. Kirchain, *Environ. Sci. Technol.*, 2012, **46**, 12986-12993.
6. R. K. Chava, J. Y. Do and M. Kang, *J. Mater. Chem. A*, 2019, **7**, 13614-13628.
7. Q. Q. Chen, X. Yang, C. C. Hou, K. Li and Y. Chen, *J. Mater. Chem. A*, 2019, **7**, 11062-11068.
8. D. Dong, Z. Wu, J. Wang, G. Fu and Y. Tang, *J. Mater. Chem. A*, 2019, **7**, 16068-16088.
9. F. Haque, A. Zavabeti, B. Y. Zhang, R. S. Datta, Y. Yin, Z. Yi, Y. Wang, N. Mahmood, N. Pillai, N. Syed, H. Khan, A. Jannat, N. Wang, N. Medhekar, K. Kalantar-Zadeh and J. Z. Ou, *J. Mater. Chem. A*, 2019, **7**, 257-268.
10. A. Hasani, M. Tekalgne, Q. V. Le, H. W. Jang and S. Y. Kim, *J. Mater. Chem. A*, 2019, **7**, 430-454.
11. I. H. Kwak, H. G. Abbas, I. S. Kwon, Y. C. Park, J. Seo, M. K. Cho, J. P. Ahn, H. W. Seo, J. Park and H. S. Kang, *J. Mater. Chem. A*, 2019, **7**, 8101-8106.
12. L. Li, C. Sun, B. Shang, Q. Li, J. Lei, N. Li and F. Pan, *J. Mater. Chem. A*, 2019, **7**, 18003-18011.
13. A. Liu, C. W. Tai, K. Holá and H. Tian, *J. Mater. Chem. A*, 2019, **7**, 4797-4803.
14. S. Liu, C. Chen, Y. Zhang, Q. Zheng, S. Zhang, X. Mu, C. Chen, J. Ma and S. Mu, *J. Mater. Chem. A*, 2019, **7**, 14466-14472.
15. C. Lv, S. Xu, Q. Yang, Z. Huang and C. Zhang, *J. Mater. Chem. A*, 2019, **7**, 12457-12467.
16. S. Niu, Y. Fang, J. Zhou, J. Cai, Y. Zang, Y. Wu, J. Ye, Y. Xie, Y. Liu, X. Zheng, W. Qu, X. Liu, G. Wang and Y. Qian, *J. Mater. Chem. A*, 2019, **7**, 10924-10929.
17. P. Vishnoi, U. Gupta, R. Pandey and C. N. R. Rao, *J. Mater. Chem. A*, 2019, **7**, 6631-6637.
18. G. Wang, J. Liu, Y. Sui, M. Wang, L. Qiao, F. Du and B. Zou, *J. Mater. Chem. A*, 2019, **7**, 14876-14881.

19. M. Wu, Y. Gong, T. Nie, J. Zhang, R. Wang, H. Wang and B. He, *J. Mater. Chem. A*, 2019, **7**, 5324-5332.
20. X. Huang, Z. Zhao, L. Cao, Y. Chen, E. Zhu, Z. Lin, M. Li, A. Yan, A. Zettl, Y. M. Wang, X. Duan, T. Mueller and Y. Huang, *Science*, 2015, **348**, 1230-1234.
21. N. K. Chaudhari, Y. Hong, B. Kim, S. I. Choi and K. Lee, *J. Mater. Chem. A*, 2019, **7**, 17183-17203.
22. Y. Cong, I. T. McCrum, X. Gao, Y. Lv, S. Miao, Z. Shao, B. Yi, H. Yu, M. J. Janik and Y. Song, *J. Mater. Chem. A*, 2019, **7**, 3161-3169.
23. S. Kühl, M. Gocyla, H. Heyen, S. Selve, M. Heggen, R. E. Dunin-Borkowski and P. Strasser, *J. Mater. Chem. A*, 2019, **7**, 1149-1159.
24. A. Kumar, X. Yang and Q. Xu, *J. Mater. Chem. A*, 2019, **7**, 112-115.
25. C. Li, Y. Xu, K. Deng, S. Yin, Z. Wang, H. Xue, X. Li, L. Wang and H. Wang, *J. Mater. Chem. A*, 2019, **7**, 3910-3916.
26. L. Wang, X. L. Tian, Y. Xu, S. Zaman, K. Qi, H. Liu and B. Y. Xia, *J. Mater. Chem. A*, 2019, **7**, 13090-13095.
27. Q. Yang, L. Shi, B. Yu, J. Xu, C. Wei, Y. Wang and H. Chen, *J. Mater. Chem. A*, 2019, **7**, 18846-18851.
28. B. W. Zhang, W. H. Lai, T. Sheng, X. M. Qu, Y. X. Wang, L. Ren, L. Zhang, Y. Du, Y. X. Jiang, S. G. Sun and S. X. Dou, *J. Mater. Chem. A*, 2019, **7**, 5214-5220.
29. C. Zhang, B. Chen, D. Mei and X. Liang, *J. Mater. Chem. A*, 2019, **7**, 5475-5481.
30. M. Shao, J. H. Odell, A. Peles and D. Su, *Chem. Commun.*, 2014, **50**, 2173-2176.
31. M. S. Kumar, D. Chen, A. Holmen and J. C. Walmsley, *Catal. Today*, 2009, **142**, 17-23.
32. J. F. Kuhmann, C.-H. Chiang, P. Harde, F. Reier, W. Österle, I. Urban and A. Klein, *Mater. Sci. Eng., A*, 1998, **242**, 22-25.
33. Z. Ma, S. Belyakov, K. Sweatman, T. Nishimura and C. Gourlay, *Nat. Commun.*, 2017, **8**, 1916.
34. B. Kempf and S. Schmauder, *Gold Bull.*, 1998, **31**, 51-57.
35. H. Okamoto, *J. Phase Equilib.*, 2003, **24**, 198-198.
36. Y. Wu, L.-L. Wang, E. Mun, D. D. Johnson, D. Mou, L. Huang, Y. Lee, S. L. Bud'ko, P. C. Canfield and A. Kaminski, *Nat. Phys.*, 2016, **12**, 667-671.
37. E. Mun, H. Ko, G. J. Miller, G. D. Samolyuk, S. L. Bud'ko and P. C. Canfield, *Phys. Rev. B*, 2012, **85**, 035135.
38. C. Kittel, *Introduction to Solid State Physics*, John Wiley & Sons, 1986.
39. G. Li, C. Fu, W. Shi, L. Jiao, J. Wu, Q. Yang, R. Saha, M. E. Kamminga, A. K. Srivastava, E. Liu, A. N. Yazdani, N. Kumar, J. Zhang, G. R. Blake, X. Liu, M. Fahlman, S. Wirth, G. Auffermann, J. Gooth, S. Parkin, V. Madhavan, X. Feng, Y. Sun and C. Felser, *Angew. Chem.*, 2019, doi:10.1002/ange.201906109.
40. D. O. Downing, Z. Liu and B. W. Eichhorn, *Polyhedron*, 2016, **103**, 66-70.
41. O. Matz and M. Calatayud, *ACS Omega*, 2018, **3**, 16063-16073.
42. F. Dogan and J. T. Vaughey, *J. Electrochem. Soc.*, 2016, **163**, A62-A66.
43. D. J. Miller, H. Öberg, S. Kaya, H. Sanchez Casalongue, D. Friebel, T. Anniyev, H. Ogasawara, H. Bluhm, L. G. M. Pettersson and A. Nilsson, *Phys. Rev. Lett.*, 2011, **107**, 195502.
44. A. Politano and G. Chiarello, *ChemCatChem*, 2016, **8**, 713–718.
45. H. Igarashi, T. Fujino, Y. Zhu, H. Uchida and M. Watanabe, *Phys. Chem. Chem. Phys.*, 2001, **3**, 306-314.
46. M. Fondell, M. Gorgoi, M. Boman and A. Lindblad, *J. Electron Spectrosc. Relat. Phenom.*, 2014, **195**, 195-199.
47. Y. Jugnet, D. Loffreda, C. l. Dupont, F. o. Delbecq, E. Ehret, F. J. Cadete Santos Aires, B. S. Mun, F. Aksoy Akgul and Z. Liu, *J. Phys. Chem. Lett.*, 2012, **3**, 3707-3714.
48. H. Ishitobi, Y. Kawatsu, Y. Kudo and N. Nakagawa, *Int. J. Hydrogen Energy*, 2018, DOI: https://doi.org/10.1016/j.ijhydene.2018.03.108, doi:10.1016/j.ijhydene.2018.1003.1108.
49. A. Cimino, D. Gazzoli and M. Valigi, *J. Electron Spectrosc. Relat. Phenom.*, 1999, **104**, 1-29.
50. W. S. Jung and B. N. Popov, *Catal. Today*, 2017, **295**, 65-74.
51. A. T. Al-Hinai, M. H. Al-Hinai and J. Dutta, *Mater. Res. Bull.*, 2014, **49**, 645-650.
52. P. Giannozzi, S. Baroni, N. Bonini, M. Calandra, R. Car, C. Cavazzoni, D. Ceresoli, G. L. Chiarotti, M. Cococcioni, I. Dabo, A. Dal Corso, S. de Gironcoli, S. Fabris, G. Fratesi, R. Gebauer, U. Gerstmann, C.

Gougoussis, A. Kokalj, L. Michele, L. Martin-Samos, N. Marzari, F. Mauri, R. Mazzarello, S. Paolini, A. Pasquarello, L. Paulatto, C. Sbraccia, S. Scandolo, G. Sclauzero, A. P. Seitsonen, A. Smogunov, P. Umari and R. M. Wentzcovitch, *J. Phys.: Condens. Matter*, 2009, **21**, 395502.
53. J. P. Perdew, K. Burke and M. Ernzerhof, *Phys. Rev. Lett.*, 1996, **77**, 3865-3868.
54. V. Barone, M. Casarin, D. Forrer, M. Pavone, M. Sambi and A. Vittadini, *J. Comput. Chem.*, 2009, **30**, 934-939.
55. D. Vanderbilt, *Phys. Rev. B*, 1990, **41**, 7892-7895.